



OPEN

Co-introduction of precipitate hardening and TRIP in a TWIP high-entropy alloy using friction stir alloying

Tianhao Wang^{1,2,5}, Shivakant Shukla^{1,3,5}, Bharat Gwalani^{1,2}, Subhasis Sinha^{1,4},
Saket Thapliyal¹, Michael Frank¹ & Rajiv S. Mishra¹✉

Tuning deformation mechanisms is imperative to overcome the well-known strength-ductility paradigm. Twinning-induced plasticity (TWIP), transformation-induced plasticity (TRIP) and precipitate hardening have been investigated separately and have been altered to achieve exceptional strength or ductility in several alloy systems. In this study, we use a novel solid-state alloying method—friction stir alloying (FSA)—to tune the microstructure, and a composition of a TWIP high-entropy alloy by adding Ti, and thus activating site-specific deformation mechanisms that occur concomitantly in a single alloy. During the FSA process, grains of the as-cast face-centered cubic matrix were refined by high-temperature severe plastic deformation and, subsequently, a new alloy composition was obtained by dissolving Ti into the matrix. After annealing the FSA specimen at 900 °C, hard Ni-Ti rich precipitates formed to strengthen the alloy. An additional result was a Ni-depleted region in the vicinity of newly-formed precipitates. The reduction in Ni locally reduced the stacking fault energy, thus inducing TRIP-based deformation while the remaining matrix still deformed as a result of TWIP. Our current approach presents a novel microstructural architecture to design alloys, an approach that combines and optimizes local compositions such that multiple deformation mechanisms can be activated to enhance engineering properties.

High-entropy alloys (HEAs) have attracted considerable interest since they were first conceptualized and synthesized by Yeh¹. This ongoing interest is due mainly to HEAs maintaining excessive entropy-driven phase stability and unique mechanical properties that include high strength at both room temperature and high temperature, good wear resistance, corrosion resistance and fatigue properties^{2,3}. HEAs also provide a completely new compositional space for designing novel materials with exceptional properties. Recent developments in the field of non-equiatomic HEAs have focused on introducing TRIP (transformation-induced plasticity)⁴, TWIP (twinning-induced plasticity)⁵, and joint activation of TWIP and TRIP^{6,7} by designing metastable alloys. Moreover, researchers have also incorporated precipitation hardening (PH)⁸ and interstitial solid solution⁷ in the HEAs as additional strengthening mechanisms. The preliminary study on TRIP-DP (dual phase)-HEA ($\text{Fe}_{50}\text{Mn}_{30}\text{Co}_{10}\text{Cr}_{10}$ at.%, γ (FCC) and ϵ (HCP) phases) by Li et al.⁴ demonstrated that both strength and ductility can be improved by a strain-induced γ to ϵ transformation. Inspired by this finding, Nene et al.⁹ modified the alloy composition by adding Si and increasing Cr ($\text{Fe}_{42}\text{Mn}_{28}\text{Co}_{10}\text{Cr}_{15}\text{Si}_5$ at.%) and thus, increasing metastability of the γ phase to capitalize on the TRIP effect. Meanwhile, Sinha et al.⁵ exchanged Co for Ni ($\text{Fe}_{42.8}\text{Mn}_{28.3}\text{Cr}_{14.8}\text{Ni}_{9.6}\text{Si}_{4.5}$ at.%) to increase the stacking fault energy to favor TWIP during plastic deformation^{10–12}. Hence, the previous work demonstrated the possibility of both TWIP and TRIP in this alloy system through compositional tuning.

Furthermore, a combined body of literature^{5–9} suggests that even minor alloying addition can greatly impact HEA strengthening mechanisms such as TRIP, TWIP and PH. Yet, the limited development of alloys can be attributed to conventional development methods that include casting, thermomechanical processing, and annealing process. In this study, friction stir alloying (FSA), a novel solid-state alloying method derived from friction stir processing (FSP)¹³, was applied for simultaneous grain refinement and alloying process. A similar approach

¹Department of Materials Science and Engineering, University of North Texas, Denton, TX 76207, USA. ²Present address: Pacific Northwest National Laboratory, Richland, WA 99352, USA. ³Present address: Oak Ridge National Laboratory, Oak Ridge, TN 37831, USA. ⁴Present address: Department of Metallurgical Engineering, IIT(BHU), Varanasi, India. ⁵These authors contributed equally: Tianhao Wang and Shivakant Shukla. ✉email: Rajiv.Mishra@unt.edu

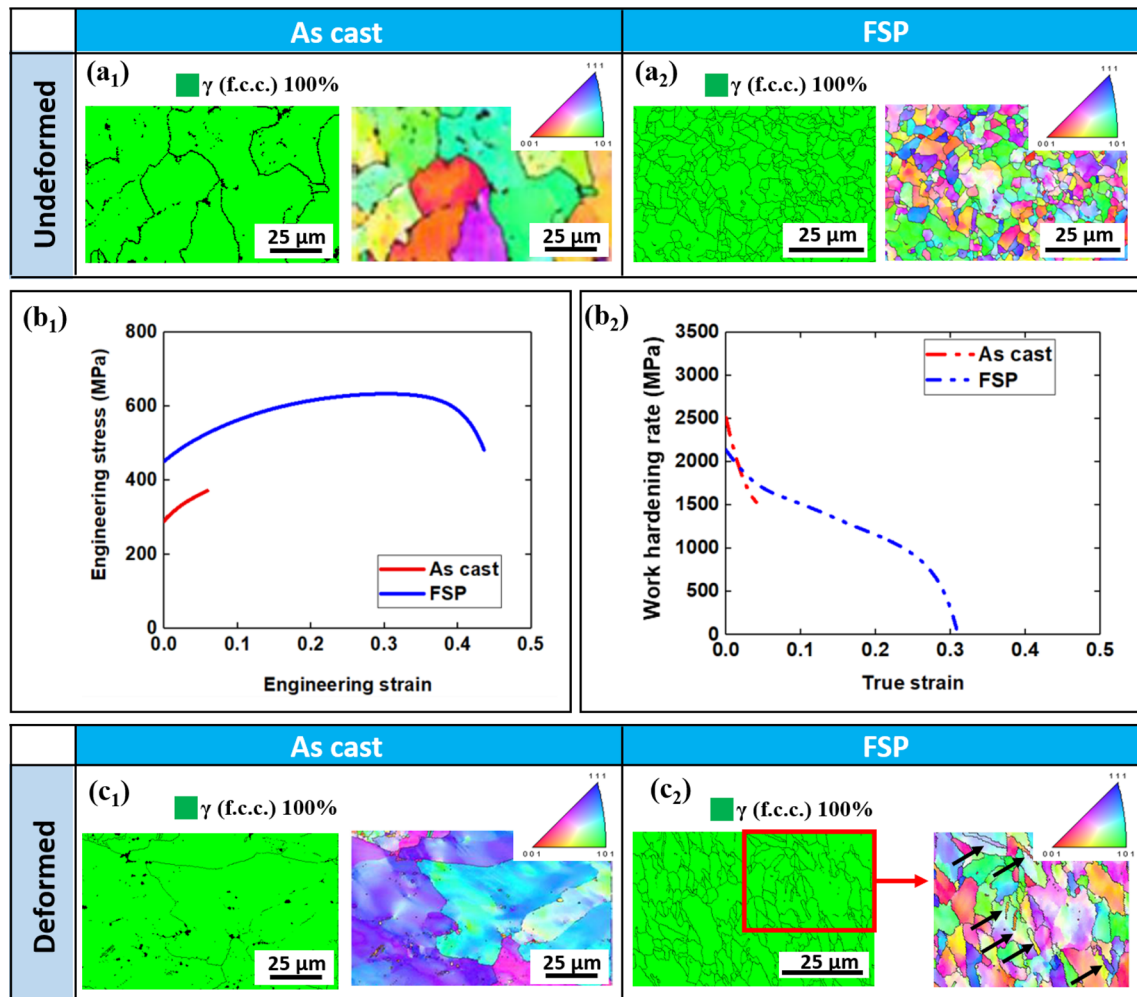


Figure 1. EBSD phase map and IPF map of (a₁) as-cast and (a₂) FSP specimen in undeformed condition; (b₁) engineering strain–stress and (b₂) work hardening rate curves of as-cast and FSP specimens under quasi static tensile testing load; EBSD phase map and IPF map of (c₁) as-cast and (c₂) FSP specimens in deformed condition. Note that deformational twins are labelled by black arrows in (c₂).

was used earlier during friction stir welding and processing where Cu¹⁴, and Fe¹⁵ powders were added during the welding and processing of Al alloys, resulting in a homogeneous distribution of intermetallic precipitates and thus enhancing mechanical properties of the processed zone. The FSA process used in the current work, utilizes the shear deformation during the solid-state processing, to distribute the additional desired alloying element into the matrix by non-equilibrium dissolution. Our previous work on non-equilibrium dissolution of Al into Al_{0.1}CoCrFeNi HEA matrix¹⁶ and that of Cu¹⁷ and V¹⁸ into TRIP HEA matrix via FSA produced encouraging results and established the viability of this process. FSA is a more efficient way to develop new alloys, especially for HEAs, since alloy modification on the existing material can be achieved without bulk melting, formation of intermetallics and cracks. Furthermore, the microstructure after FSA (or any friction-stir-based technique) is predominantly recrystallized and hence requires no further processing (such as rolling or heat-treatment), as a result of the synergistic effects of strain, strain rate and temperature on microstructural modification. Note that FSA is a local alloying technique which cannot produce bulk materials, but upscaling of such a process is achievable by using the emerging friction-based manufacturing techniques¹⁹.

In the current study, we selected Fe_{42.8}Mn_{28.3}Cr_{14.8}Ni_{9.6}Si_{4.5} at.% (Ni–Si5–HEA) as the starting material and alloyed Ti using FSA. The alloying of Ti resulted in formation of Ni₃Ti precipitates which, on one hand, strengthened the material; and, consequently, they also reduced Ni concentration around Ni₃Ti precipitates, thus lowering the SFE enough to introduce an additional TRIP mechanism effect locally.

Results and discussion

Benchmark from FSP. Figure 1(a₁–a₂) display the microstructural variation in as-cast and FSP conditions. EBSD phase maps confirm that both as-cast and FSP conditions consist of a single phase of γ , which indicates that no phase transformation occurred during FSP. Grain refinement was observed after FSP as the average grain size of $13.7 \pm 2.5 \mu\text{m}$ in as-cast condition reduced to $1.8 \pm 0.6 \mu\text{m}$ in FSP condition. Mechanical behavior includes

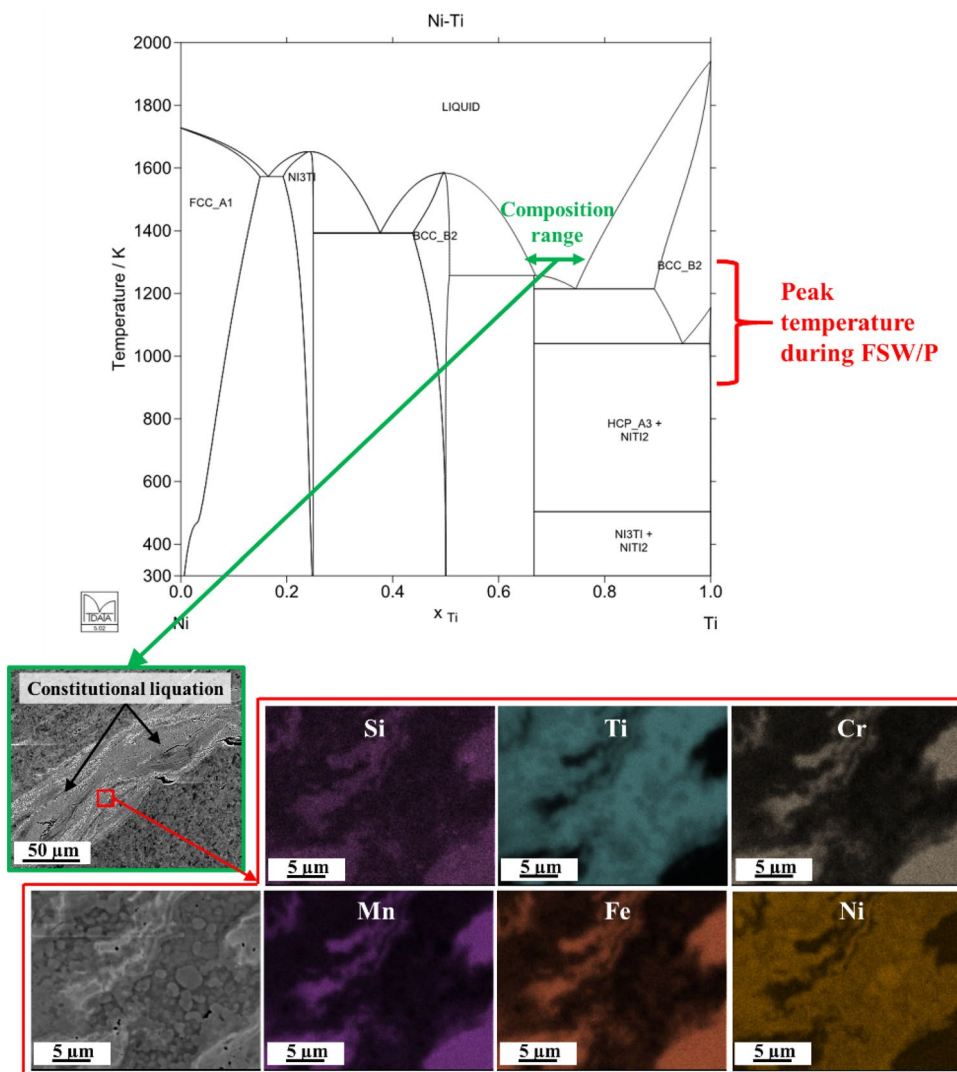


Figure 2. Phase diagram of Ni-Ti and SEM image and EDS map on processed region after one pass FSA displaying that constitutional liquation occurred during FSA.

engineering stress-strain curves and work hardening rate of as-cast and FSP specimens (Fig. 1(b₁-b₂)). Yield strength, tensile strength and ductility increased from ~ 288 MPa, ~ 367 MPa and ~ 6% in the as-cast condition to ~ 451 MPa, ~ 645 MPa and ~ 43% in the FSP condition (Fig. 1(b₁)). The decelerating trend in work hardening rate of FSP condition suggests that no phase transformation (TRIP) occurred during testing (Fig. 1(b₂)). Also, there is no clear trend of work hardening rate of as-cast condition since it had limited ductility and early failure due to its coarse-grained structure (Fig. 1(b₂)).

Figure 1(c₁,c₂) display the microstructural response of as-cast and FSP specimens in deformed condition. Note that the scans were taken near the fracture tip. Phase maps of both as-cast and FSP conditions after deformation confirmed that no phase transformation had occurred, thereby indicating that TRIP had not occurred. In addition, the inverse pole figure (IPF) maps of deformed FSP specimen show that deformation twins (labelled by black arrow in Fig. 1(c₂)) formed during loading. While coarse grain size favors twinning, the lack of evidence of deformation twins in the deformed as-cast specimen might be due to the limited number of grains in the gauge section of the as-cast condition. Hence strain hardening behavior would be dependent on the orientation of the individual grains with respect to the loading axis. For the present study, limited strain seems to have been accommodated by the as-cast microstructure by the onset of TWIP before crack and fracture. Therefore, improvement in mechanical properties of the FSP condition can be attributed to grain refinement and TWIP.

Parameter optimization for FSA. We initially used a high tool rotation rate (600 RPM) to increase strain, strain rate and temperature in order to promote dissolution of Ti into the FCC matrix. However, somewhat unexpectedly, excessive heat was produced during processing. Local melting of Ti was observed in the processed region (SEM images of Fig. 2). Previous studies confirmed that peak temperature during friction stir welding/processing on steels ranged from ~ 900 to 1300 K^{20–23}. We assumed that the peak temperature during

Condition	Rotation rate (RPM)	Traverse speed (mm/min)
FSP		
First pass	650	50.8
Second pass	350	50.8
FSA		
First pass	150	50.8
Second pass	150	50.8

Table 1. Critical process parameters applied for FSP and FSA process.

FSA of Ni–Si5–HEA would also fall in the same range since Fe content is near 40 at.% in the matrix. The peak temperature during the FSA process being lower than the melting point of Ti by ~ 600–1000 K (phase diagram in Fig. 2) implies that constitutional liquation occurred when Ti and Ni mixed in a certain compositional ratio (composition range labelled in the phase diagram in Fig. 2).

Similar to observations in the present study, Sato et al.²⁴ reported that constitutional liquation occurred between friction stir welding (FSW) of aluminum and magnesium alloys at excessive temperatures. Therefore, determining welding parameters that would generate lower heat during FSA is desirable. Previous researchers correlated the FSW parameters with non-dimensional peak temperature T^* ²⁵ according to Eq. (1) and the constants of α and β have been reported as 0.151 and 0.097, respectively, which fit well with various aluminum alloys and steels based on the data reported in²⁶. Hence, we have assumed the values of these constants for our HEA to be similar to the above-mentioned conventional alloys for this study.

$$T^* = \alpha \log_{10}(Q^*) + \beta \quad (1)$$

The non-dimensional peak temperature, T^* , is defined in Eq. (2)²⁵. Q^* is the non-dimensional heat input defined in Eq. (3)²⁵.

$$T^* = \frac{T_p - T_{in}}{T_s - T_{in}} \quad (2)$$

$$Q^* = \frac{\sigma_8 A \omega C_p \phi}{k U^2} \quad (3)$$

where T_p is peak temperature, T_{in} is initial temperature and T_s is solidus temperature, σ_8 is yield stress of the material at a temperature of 80% of solidus temperature of the material ($0.8T_s$), A is the cross-sectional area of the tool shoulder, ω is tool rotational velocity, U is traverse speed, C_p is the specific heat capacity, ϕ is the ratio based on heat transfer between tool and workpiece, and k is thermal conductivity of the workpiece. Various parameters and coefficients need to be provided to calculate actual peak temperature, T_p , during FSW for a given welding setup, including FSW tool dimensions, welding parameters and physical properties of the base material and tool. If welding parameters are the only variables with constant FSW tool and base material properties, the change in peak temperature can be simplified and calculated via Eq. (4), which was obtained through Eqs. (1)–(3).

$$T_p(1) - T_p(2) = \alpha \log_{10} \left(\frac{\omega(1) U(2)^2}{\omega(2) U(1)^2} \right) (T_s - T_{in}) \quad (4)$$

We assumed the solidus temperature of the alloy (T_s) as ~ 1200 °C, and T_{in} equals 25 °C (ambient temperature). By reducing the tool rotation rate (ω) from 600 to 150 RPM along with a constant traverse speed of 50.8 mm/min, peak temperature reduced by ~ 130 °C. Combined with the fact that peak temperature during friction stir welding/processing generally ranged from 900 to 1300 K, the peak temperature during optimized FSA process (rotation rate of 150 RPM) is assumed to be lower than ~ 1200 °C (lower than constitutional liquation temperature of Ni–Ti system). Furthermore, the observation of no solidification features at 150 RPM indicated that the reduction of peak temperature by 130 °C was sufficient to avoid constitutional liquation between Ti and Ni originating from Ni–Si5–HEA matrix during FSA. Therefore, two-pass FSA with tool rotation rate of 150 RPM was conducted to dissolve Ti while avoiding constitutional liquation. EDS analysis was conducted on nugget region of double-pass FSA condition to demonstrate element distribution (see Supplementary Fig. 2). Compared with as-cast condition, elements of Cr, Mn, Fe and Ni are more homogenized, Si–Mn–Ni-rich phases were replaced with much finer Si-rich phases, and Ti was dissolved into matrix in FSA condition.

FSA and FSA+Anneal. FSA was conducted with optimized parameters as listed in Table 1. Then, microstructural analysis using orientation microscopy of before-and-after tensile testing was conducted on FSA specimens (Fig. 3(a₁,c₁)). The phase map of the deformed FSA specimen did not show any significant evidence of stress-induced phase transformation (TRIP effect); however, deformation twins (TWIP) can be observed in the IPF map of the deformed FSA specimen (Fig. 3(c₁)). Yield strength (~ 554 MPa) and tensile strength (~ 725 MPa) of FSA specimens are both higher than the FSP condition. This is because the grain size ($1.2 \pm 0.5 \mu\text{m}$) in the FSA condition with lower rotation rate and heat input was finer than that in the FSP condition. A similar trend

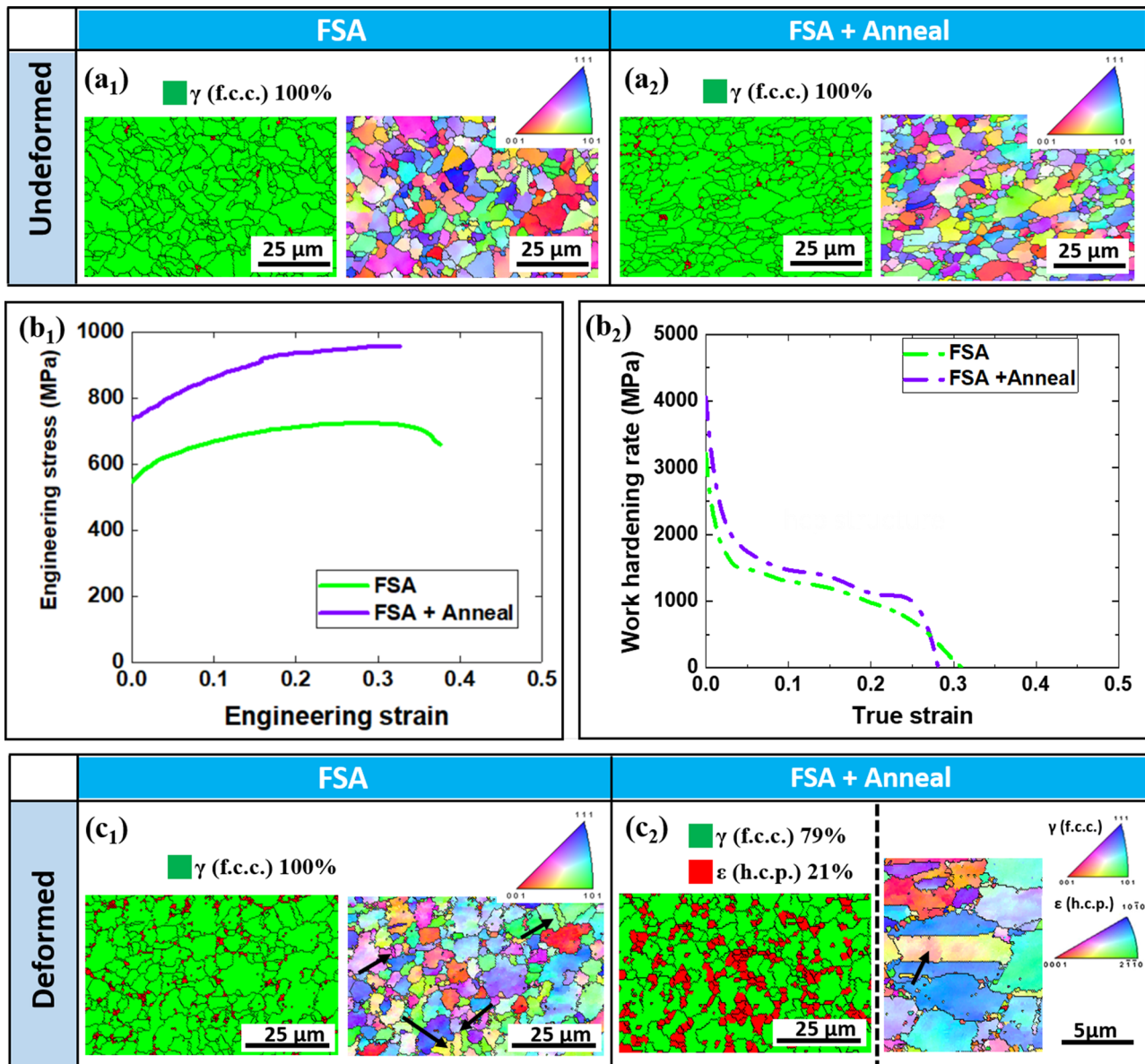


Figure 3. EBSD phase map and IPF map of (a₁) FSA and (a₂) FSA + Anneal specimens in undeformed condition; (b₁) engineering strain–stress and (b₂) work hardening rate curves of FSA and FSA + Anneal specimens under quasi static tensile testing load; EBSD phase map and IPF map of (c₁) FSA and (c₂) FSA + Anneal specimens in deformed condition. Note that deformational twins are labelled by black arrows in (c₁ and c₂). Also note that the red color displayed in phase map of (a₁), (a₂) and (c₁) represent regions with low confidence indexes values rather than ϵ (HCP) phases.

of work hardening rate in the FSA specimen as compared to the FSP specimen from tensile testing response also suggests that TRIP was not triggered during testing of FSA specimens (Fig. 3(b₂)). The additional annealing step was done resulting in the precipitation of Ni₃Ti phase as confirmed in Fig. 4(a). The precipitation of this Ni enriched intermetallic phase may result in lowering of Ni concentration in the matrix surrounding these precipitates. The reduction Ni concentration can result in lowering of the stacking fault energy of the matrix and just increase the possibility of deformation by TRIP. Note that after annealing at 900 °C for 4 h, we did not observe significant grain coarsening or phase changes in the microstructure (Fig. 3(a₂)). Yield strength and tensile strength of FSA + Anneal specimen are enhanced to ~736 MPa and ~958 MPa, respectively (Fig. 3(b₁)). Meanwhile, work hardening rate of the FSA + Anneal specimen being more sustained as compared with those of FSA and FSP conditions (Fig. 3(b₂)) suggests the possibility of an additional mechanism (TRIP) while deformation in the FSA + Anneal specimen during loading. Figure 3(c₂) presents 21% of $\gamma \rightarrow \epsilon$ transformation (TRIP) and deformation twins (TWIP) of the FSA + Anneal specimen via EBSD phase map and IPF map, respectively.

To further substantiate the proposed hypothesis, a detailed TEM analysis of the final condition (i.e., FSA + Anneal) specimen was conducted. The results of both pre- and post-deformation TEM analyses are presented in Fig. 4. A high annular angle dark field scanning TEM (HAADF STEM) image of the pre-deformed

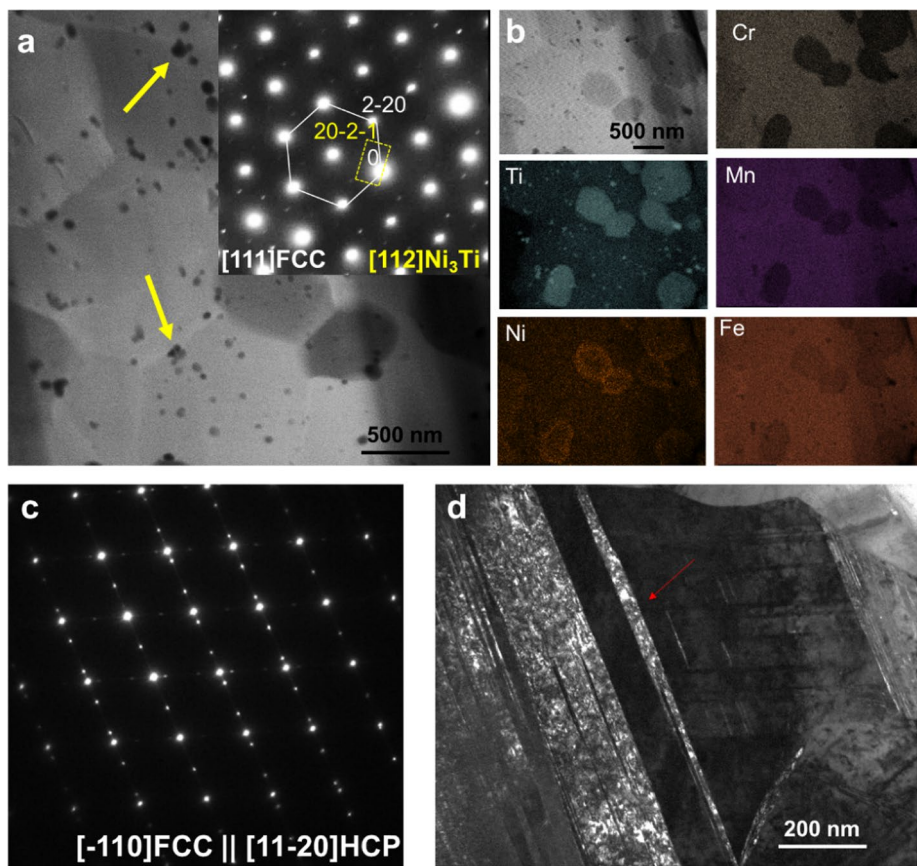


Figure 4. (a) HAADF-STEM image and corresponding SAED showing Ni₃Ti precipitates indicated via yellow arrows after annealing and (b) corresponding TEM-EDS analysis revealing the presence of Ti and Ni rich precipitates. (c) Post-deformation SAED indicating the orientation relationship between $< \bar{1}\bar{1}0 >_{fcc}$ and $< 1\bar{1}20 >_{hcp}$ and (d) BF-TEM showing transformation induced nano-scale HCP phases indicated via red arrows.

sample shows the fine-grained structure with dark contrast precipitates (Fig. 4(a)). In addition to a high density of extremely fine precipitates (~ 5 nm), some large second-phase grains were present. The corresponding selected area electron diffraction (SAED) pattern was recorded along [111]_{fcc} zone axis (Fig. 4 (a) inset). Note that the extra reflections in the SAED pattern were consistently indexed to be [112] Ni₃Ti phase based on a D0₂₄ structure. The precipitates were further characterized using EDS. Precipitates rich in Ti and Ni were clearly visible in the TEM-EDS analysis of the pre-deformed specimen (Fig. 4(b)), and hence the depletion of Ni from the matrix was achieved via annealing treatment once the matrix was saturated with Ti during FSA. The evolution of deformation structure on the tensile tested sample is presented in Fig. 4(c),(d). The SAED pattern of the deformed specimen (Fig. 4(c)) clearly demonstrates a well-recognized orientation-relationship (OR) of FCC \rightarrow HCP transformation, also known as Shoji-Nishiyama OR, where $< \bar{1}\bar{1}0 >_{fcc}$ is parallel to $< 1\bar{1}20 >_{hcp}$. The corresponding dark field TEM (DF-TEM) image in Fig. 4(d) also reveals the presence of HCP phase lamellae in FCC matrix. Previous studies^{27–29} have established that in metastable FCC alloys, the formation of HCP lamellae is expected during deformation. Hence, the final microstructural condition was tuned to demonstrate the deformation-induced transformation of FCC to HCP phase.

A possible mechanism and procedure of FSA is summarized schematically in Fig. 5. Idrissi³⁰ reported that the activated plasticity mode is highly dependent on SFE values. With decreasing SFE, the observed deformation mode is well-known to be transition from dislocation glide to mechanical twinning and finally to martensitic phase transformation³¹. Generally, deformation-induced martensitic transformation is triggered when $SFE < 15 \text{ mJ m}^{-2}$ ³², mechanical twinning is triggered when $20 \text{ mJ m}^{-2} < SFE < 40 \text{ mJ m}^{-2}$, and dislocation glide becomes the predominant plastic deformation mode when $SFE > 40 \text{ mJ m}^{-2}$ ³³. According to previous literature^{30–33}, SFE of Ni-Si5-HEA should lie within $20–40 \text{ mJ m}^{-2}$, based on the absence of phase transformation during straining. By introducing Ti into the system, Ni was preferentially depleted from the matrix. As a result, local reduction in SFE was expected locally below $15–20 \text{ mJ m}^{-2}$, enabling the onset of TRIP during tensile deformation. In addition to activation of TRIP as a strengthening mechanism, the newly-formed Ni₃Ti precipitates also act as obstacles to dislocation glide during mechanical deformation. Meanwhile, TWIP was maintained during mechanical deformation since a certain amount of Ni was left in the remaining matrix. Local changes

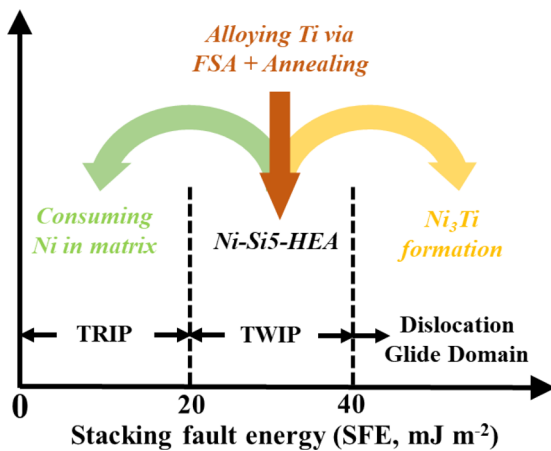


Figure 5. Schematic showing the proposed tuning pathway via FSA.

are expected to have led to the changes deformation mechanisms, thus we evaluated the resultant deformation behavior on work hardening behavior was observed to change.

To correlate the work hardening behavior, a strength model recently developed by Lloyd et al. was employed to correlate work hardening behavior with expected SFE. Four parameters were developed to model the strain hardening behaviors of TRIP and TWIP steels³⁴. One of the four parameters θ_0 was shown to be related to the SFE, by the relationship shown in Eq. (5):

$$\theta_0 = 17500 \times (\text{SFE} + 5.0)^{-0.6} \quad (5)$$

Therefore, in this study, the four parameters of the model were tuned to fit the experimental stress-strain behaviors of the FSP and the FSA + Anneal conditions of Ni-Si5-HEA. By comparison, another TRIP-HEA (CS-HEA³⁵) with similar chemical composition was also investigated. The experimental stress-strain curves and fitting curves are shown in Fig. 6(a). θ_0 for CS-HEA after FSP, Ni-Si5-HEA after FSP, and Ni-Si5-HEA after FSA + Anneal is 5000, 2000 and 3000, respectively. Comparing θ_0 of TRIP and TWIP HEAs with TWIP and TRIP steels, the estimated SFE of Ni-Si5-HEA after FSP and FSA + Anneal are shown in Fig. 6(b). Note that the estimated SFE of CS-HEA after FSP is between 0 and 10, which agrees with measured SFE of CS-HEA though neutron diffraction³⁵.

Conclusions

A novel solid-state alloying method—friction stir alloying (FSA)—was applied to introduce Ti into a TWIP HEA. The conclusions are:

- FSA parameter optimization was achieved by reducing tool rotation rate to 150 RPM Ni-Ti constitutional liquation during FSA. Subsequently, Ti was successfully dissolved into the Ni-Si5-HEA matrix during FSA.
- Annealing of the FSA specimens led to the formation of Ni₃Ti precipitates so that precipitation hardening was introduced in this alloy system.
- Formation of Ni₃Ti precipitates facilitated a Ni-depleted region in the vicinity, which enabled TRIP locally.
- Transformation pathway under strain was modified from stand-alone TWIP in the base material to TWIP + TRIP + PH in the FSA + Anneal specimen.
- Deformation behavior correlates well with SFE predicted by stress-strain response based on experimental observations of TWIP and TRIP.

Materials and methods

Materials. The starting material is as-cast Ni-Si5-HEA (Fe_{42.8}Mn_{28.3}Cr_{14.8}Ni_{9.6}Si_{4.5} at.%). The alloy was produced by vacuum arc-casting in a cold copper crucible, using pure metal powders and ingot dimensions of 300 × 100 × 6 mm³. The chamber was backfilled with argon to 1 atm. prior to each melt. The microstructure of as-cast Ni-Si5-HEA is detailed in Supplementary Fig. 1. As-cast Ni-Si5-HEA consists of a single γ (FCC) phase (Supplementary Fig. 1 (a)), but inhomogeneity in alloying elements exists. Apart from the matrix, Si-Mn-Ni-rich and Cr-Fe-lean phases (labelled by yellow circles) and Cr-rich and Ni-lean phases (labelled by green circles) were observed (Supplementary Fig. 1 (b)).

Methods. The influence of FSP and additional alloying of Ti were differentiated by stand-alone FSP on the Ni-Si5-HEA (parameters listed in Table 1). As for the FSA process, pre-drilled holes of diameter 0.6 mm, depth 3.0 mm and gap 1.0 mm along the tool traverse direction were introduced via drilling on the as-cast Ni-Si5-HEA sheet. Ti powders of 99.9% purity and ~ 10 μm average particle size were filled into these pre-drilled holes. Note that the volume percentage of holes to processed region was ~ 5%. According to the chemical composition of base Ni-Si5-HEA (Fe_{42.8}Mn_{28.3}Cr_{14.8}Ni_{9.6}Si_{4.5} at.%), the density of base Ni-Si5-HEA is calculated as ~ 7.3 g/cc.

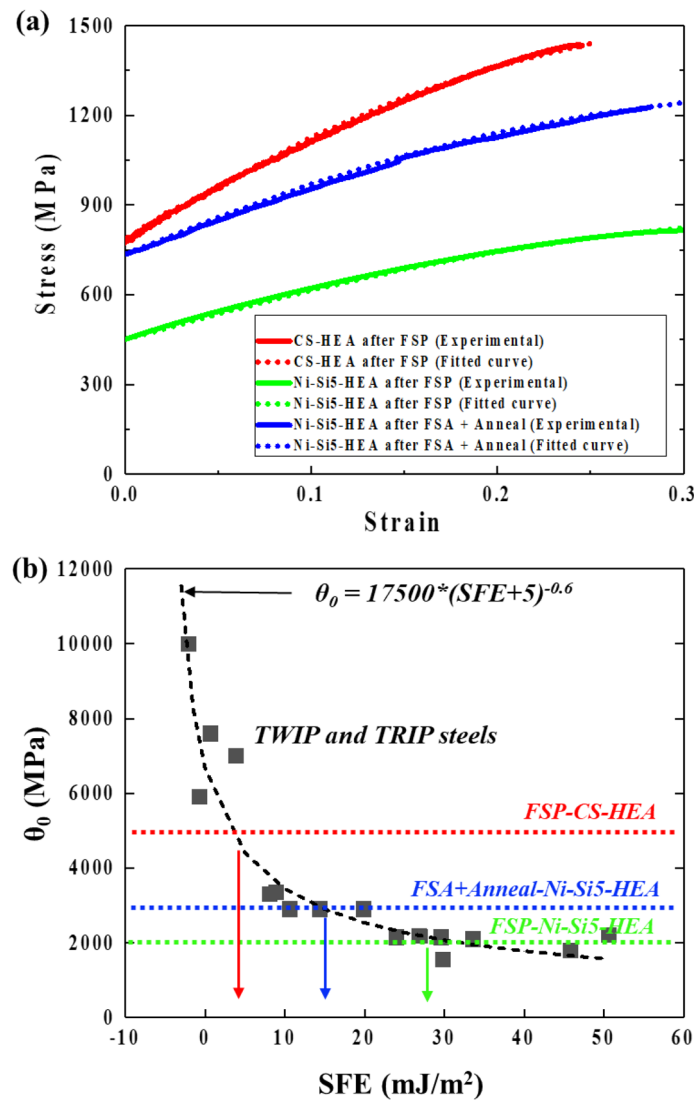


Figure 6. (a) Experimental stress–strain curves of CS–HEA and Ni–Si5–HEA in different conditions, (b) Correlations of θ_0 and SFE for TRIP and TWIP steels.

The density of Ti is ~ 4.5 g/cc, therefore, the volume fraction of Ti being 5% can be transferred to be mass fraction of Ti being $\sim 3.1\%$. The nominal chemical composition of FSA (or FSA + Anneal) condition is: Fe_{41.3} Mn_{27.3} Cr_{14.3} Ni_{9.3} Si_{4.3} Ti_{3.5} at.%. Afterwards, the rotating tool traversed along the pre-drilled holes filled with Ti powders. The parameters of FSA are also listed in Table 1. Differences in parameters between FSP and FSA are explained in the section *Parameter Optimization for FSA*. A W-Re based tool was used for both FSP and FSA. Pin length, pin diameter at root and tip, and shoulder diameter were 3.8 mm, 7.6 mm, 5.0 mm, and 16.0 mm, respectively. Plunge depth is 4.0 mm for both FSP and FSA process. In addition, an annealing process was conducted on FSA specimens so that Ni₃Ti precipitates formed along with the consumption of Ni in the matrix of the FSA specimen. Annealing temperature and time were 900 °C and 4 h, respectively.

Both microstructural evolution and mechanical behavior were included in this study. Transverse cross sections of processed volume were cut by electrical discharge machining and were final-polished to 0.02 μm surface finish with colloidal silica suspension. Scanning electron microscopy (SEM), energy-dispersive X-ray spectroscopy (EDS) and electron backscattered diffraction (EBSD) analyses were carried out using FEI Nova NanoSEM 230 with EDAX Octane Elite EDS and Hikari Super EBSD detector, respectively. The SEM imaging and EDS analysis were performed at an accelerating voltage of 15 kV while EBSD analysis was performed with a step size of 0.05 μm. Lift-out samples for transmission electron microscopy (TEM) were prepared using a FEI Nova 200 dual beam focused ion beam (FIB). TEM analysis was carried out on Tecnai G2 F20 S-Twin TEM operating at 200 kV. Mini-tensile testing on as-cast material, FSP and FSA specimens was conducted at initial strain rate of 0.001 s⁻¹. Width, thickness and gauge length of the specimens were 1.0, 1.0, and 5.0 mm, respectively. Mini-tensile specimens were taken from 1 mm below the surface of the processed nugget region. To maintain statistical accuracy, three specimens were tested for each condition.

Data availability

The raw/processed data required to reproduce these findings cannot be shared at this time as the data also forms part of an ongoing study.

Received: 12 October 2020; Accepted: 4 January 2021

Published online: 15 January 2021

References

- Yeh, J. et al. Nanostructured high-entropy alloys with multiple principal elements: novel alloy design concepts and outcomes. *Adv. Eng. Mater.* **6**(5), 299–303 (2004).
- Tsai, M. & Yeh, J. High-entropy alloys: A critical review. *Mater. Res. Lett.* **2**(3), 107–123 (2014).
- Shukla, S., Wang, T., Cotton, S. & Mishra, R. S. Hierarchical microstructure for improved fatigue properties in a eutectic high entropy alloy. *Scr. Mater.* **156**, 105–109 (2018).
- Li, Z., Pradeep, K. G., Deng, Y., Raabe, D. & Tasan, C. C. Metastable high-entropy dual-phase alloys overcome the strength–ductility trade-off. *Nature* **534**(7606), 227 (2016).
- Sinha, S. et al. Microstructural evolution and deformation behavior of Ni–Si- and Co–Si-containing metastable high entropy alloys. *Metall. Mater. Trans. A* <https://doi.org/10.1007/s11661-018-4968-6> (2018).
- Su, J., Raabe, D. & Li, Z. Hierarchical microstructure design to tune the mechanical behavior of an interstitial TRIP-TWIP high-entropy alloy. *Acta Mater.* **163**, 40–54 (2019).
- Li, Z., Tasan, C. C., Springer, H., Gault, B. & Raabe, D. Interstitial atoms enable joint twinning and transformation induced plasticity in strong and ductile high-entropy alloys. *Nat. Publ. Gr.* <https://doi.org/10.1038/srep40704> (2017).
- He, J. Y. et al. A precipitation-hardened high-entropy alloy with outstanding tensile properties. *Acta Mater.* **102**, 187–196 (2016).
- Nene, S. S. et al. Extremely high strength and work hardening ability in a metastable high entropy alloy. *Sci. Rep.* **8**(1), 9920 (2018).
- Charnock, W. & Nutting, J. The effect of carbon and nickel upon the stacking-fault energy of iron. *Met. Sci. J.* **1**(1), 123–127 (1967).
- Liu, S. F. et al. Stacking fault energy of face-centered-cubic high entropy alloys. *Intermetallics* **93**, 269–273 (2018).
- Zaddach, A. J., Niu, C., Koch, C. C. & Irving, D. L. Mechanical properties and stacking fault energies of NiFeCrCoMn high-entropy alloy. *JOM* **65**(12), 1780–1789 (2013).
- Mishra, R. S. & Ma, Z. Y. Friction stir welding and processing. *Mater. Sci. Eng. R Rep.* **50**(1–2), 1–78 (2005).
- Inada, K., Fujii, H., Ji, Y. S., Sun, Y. F. & Morisada, Y. Effect of gap on FSW joint formation and development of friction powder processing. *Sci. Technol. Weld. Join.* **15**(2), 131–136 (2010).
- Fujii, H. et al. Fabrication of Fe-based metallic glass particle reinforced Al-based composite materials by friction stir processing. *Mater. Trans.* **52**(8), 1634–1640 (2011).
- Wang, T., Shukla, S., Komarasamy, M., Liu, K. & Mishra, R. S. Towards heterogeneous $\text{Al}_x\text{CoCrFeNi}$ high entropy alloy via friction stir processing. *Mater. Lett.* **236**, 472–475 (2019).
- Shukla, S. et al. Friction stir gradient alloying: A novel solid-state high throughput screening technique for high entropy alloys. *Mater. Today Commun.* **23**, 100869 (2019).
- Agrawal, P., Shukla, S., Gupta, S., Agrawal, P. & Mishra, R. S. Friction stir gradient alloying: a high-throughput method to explore the influence of V in enabling HCP to BCC transformation in a γ -FCC dominated high entropy alloy. *Appl. Mater. Today* **21**, 100853 (2020).
- Yu, H. Z. & Mishra, R. S. Additive friction stir deposition: a deformation processing route to metal additive manufacturing. *Mater. Res. Lett.* **9**(2), 71–83 (2020).
- Nandan, R., G. G. R., Roy, G. G., Lienert, T. J. & Debroy, T. Three-dimensional heat and material flow during friction stir welding of mild steel. *Acta Mater.* **55**(3), 883–895 (2007).
- Fujii, H. et al. Friction stir welding of carbon steels. *Mater. Sci. Eng. A* **429**(1–2), 50–57 (2006).
- Tungala, V. et al. Microstructure and mechanical properties of friction stir processed cast Eglin steel (ES-1). *Mater. Sci. Eng., A* **709**, 105–114 (2018).
- Manvatkar, V., De, A., Svensson, L. E. & DebRoy, T. Cooling rates and peak temperatures during friction stir welding of a high-carbon steel. *Scr. Mater.* **94**, 36–39 (2015).
- Sato, Y. S., Park, S. H. C., Michiuchi, M. & Kokawa, H. Constitutional liquation during dissimilar friction stir welding of Al and Mg alloys. *Scr. Mater.* **50**(9), 1233–1236 (2004).
- Roy, G. G., Nandan, R. & DebRoy, T. Dimensionless correlation to estimate peak temperature during friction stir welding. *Sci. Technol. Weld. Join.* **11**(5), 606–608 (2006).
- Arora, A., DebRoy, T. & Bhadeshia, H. K. D. H. Back-of-the-envelope calculations in friction stir welding—velocities, peak temperature, torque, and hardness. *Acta Mater.* **59**(5), 2020–2028 (2011).
- Yang, J. X., Zhao, H. L., Gong, H. R., Song, M. & Ren, Q. Q. Proposed mechanism of HCP→ FCC phase transition in titanium through first principles calculation and experiments. *Scientific Reports* **8**(1), 1–9 (2018).
- Miao, J. et al. The evolution of the deformation substructure in a Ni–Co–Cr equiatomic solid solution alloy. *Acta Mater.* **132**, 35–48 (2017).
- Niu, C., LaRosa, C. R., Miao, J., Mills, M. J. & Ghazisaeidi, M. Magnetically-driven phase transformation strengthening in high entropy alloys. *Nat. Commun.* **9**(1), 1–9 (2018).
- Idrissi, H., Ryelandt, L., Veron, M., Schryvers, D. & Jacques, P. J. Is there a relationship between the stacking fault character and the activated mode of plasticity of Fe–Mn-based austenitic steels?. *Scr. Mater.* **60**(11), 941–944 (2009).
- Curtze, S. & Kuokkala, V. T. Dependence of tensile deformation behavior of TWIP steels on stacking fault energy, temperature and strain rate. *Acta Mater.* **58**(15), 5129–5141 (2010).
- De Cooman, B. C., Estrin, Y. & Kim, S. K. Twinning-induced plasticity (TWIP) steels. *Acta Mater.* **142**, 283–362 (2018).
- Allain, S., Chateau, J. P., Bouaziz, O., Migot, S. & Guelton, N. Correlations between the calculated stacking fault energy and the plasticity mechanisms in Fe–Mn–C alloys. *Mater. Sci. Eng. A* **387**, 158–162 (2004).
- Lloyd, J. T., Field, D. M. & Limmer, K. R. A four parameter hardening model for TWIP and TRIP steels. *Mater. Des.* **194**, 108878 (2020).
- Frank, M. et al. Investigating the deformation mechanisms of a highly metastable high entropy alloy using in-situ neutron diffraction. *Mater. Today Commun.* **23**, 100858 (2020).

Acknowledgements

The work was performed under a cooperative agreement between the Army Research Laboratory and the University of North Texas (W911NF-18-2-0067) and the National Science Foundation (NSF) Grant 1435810. The authors acknowledge Materials Research Facilities (MRF) at University of North Texas for the use of microscopy equipment.

Author contributions

R.S.M. designed the work. T.W. and S.S. conducted the processing and heat treatment experiments. S.S. and B.G. conducted the TEM experiments and analyzed the data. S.S. conducted the EBSD experiments and analyzed the data. S.T. and M.F. conducted the mechanical testing experiments and analyzed the data. T.W., S.S., B.G. and R.S.M. drafted the manuscript and all the authors contributed to the final paper.

Competing interests

The authors declare no competing interests.

Additional information

Supplementary Information The online version contains supplementary material available at <https://doi.org/10.1038/s41598-021-81350-0>.

Correspondence and requests for materials should be addressed to R.S.M.

Reprints and permissions information is available at www.nature.com/reprints.

Publisher's note Springer Nature remains neutral with regard to jurisdictional claims in published maps and institutional affiliations.



Open Access This article is licensed under a Creative Commons Attribution 4.0 International License, which permits use, sharing, adaptation, distribution and reproduction in any medium or format, as long as you give appropriate credit to the original author(s) and the source, provide a link to the Creative Commons licence, and indicate if changes were made. The images or other third party material in this article are included in the article's Creative Commons licence, unless indicated otherwise in a credit line to the material. If material is not included in the article's Creative Commons licence and your intended use is not permitted by statutory regulation or exceeds the permitted use, you will need to obtain permission directly from the copyright holder. To view a copy of this licence, visit <http://creativecommons.org/licenses/by/4.0/>.

© The Author(s) 2021